



**HAL**  
open science

## Chemical Bath Deposition of ZnO Nanowires Using Copper Nitrate as an Additive for Compensating Doping

Clément Lausecker, Bassem Salem, Xavier Baillin, Odette Chaix-Pluchery, Herve Roussel, Sébastien Labau, Bernard Pelissier, Estelle Appert, Vincent Consonni

► **To cite this version:**

Clément Lausecker, Bassem Salem, Xavier Baillin, Odette Chaix-Pluchery, Herve Roussel, et al.. Chemical Bath Deposition of ZnO Nanowires Using Copper Nitrate as an Additive for Compensating Doping. *Inorganic Chemistry*, 2021, 60 (3), pp.1612-1623. 10.1021/acs.inorgchem.0c03086 . hal-03131100

**HAL Id: hal-03131100**

**<https://hal.science/hal-03131100>**

Submitted on 4 Feb 2021

**HAL** is a multi-disciplinary open access archive for the deposit and dissemination of scientific research documents, whether they are published or not. The documents may come from teaching and research institutions in France or abroad, or from public or private research centers.

L'archive ouverte pluridisciplinaire **HAL**, est destinée au dépôt et à la diffusion de documents scientifiques de niveau recherche, publiés ou non, émanant des établissements d'enseignement et de recherche français ou étrangers, des laboratoires publics ou privés.

# Chemical Bath Deposition of ZnO Nanowires Using Copper Nitrate as an Additive for Compensating Doping

*Clément Lausecker,<sup>1,2,3</sup> Bassem Salem,<sup>\*2</sup> Xavier Baillin,<sup>3</sup> Odette Chaix-Pluchery,<sup>1</sup> Hervé Roussel,<sup>1</sup>  
Sébastien Labau,<sup>2</sup> Bernard Pelissier,<sup>2</sup> Estelle Appert,<sup>1</sup> and Vincent Consonni<sup>\*1</sup>*

<sup>1</sup> Univ. Grenoble Alpes, CNRS, Grenoble INP, LMGP, F-38016 Grenoble, France

<sup>2</sup> Univ. Grenoble Alpes, CNRS, CEA/LETI-Minatec, Grenoble INP, LTM, F-38054 Grenoble, France

<sup>3</sup> Univ. Grenoble Alpes, CEA, LETI, F-38054 Grenoble, France

## ABSTRACT

The controlled incorporation of dopants like copper into ZnO nanowires (NWs) grown by chemical bath deposition (CBD) is still challenging despite its critical importance for the development of piezoelectric devices. In this context, the effects of the addition of copper nitrate during the CBD of ZnO NWs grown on Au seed layers are investigated in detail, where zinc nitrate and hexamethylenetetramine are used as standard chemical precursors and ammonia as an additive to tune the pH. By combining thermodynamic simulations with chemical and structural analyses, we show that copper oxide nanocrystals simultaneously form with ZnO NWs during the CBD process in the low-pH region associated with a large supersaturation of Cu species. The Cu(II) and Zn(II) speciation diagrams reveal that both species show very similar behaviors, as they predominantly form either  $X^{2+}$  ions (with  $X = \text{Cu}$  or  $\text{Zn}$ ) or  $X(\text{NH}_3)_4^{2+}$  ion complexes, depending on the pH value. Owing to their similar ionic structures,  $\text{Cu}^{2+}$  and  $\text{Cu}(\text{NH}_3)_4^{2+}$  ions preferentially formed in the low- and high-pH regions, respectively, are able to compete with the corresponding  $\text{Zn}^{2+}$  and  $\text{Zn}(\text{NH}_3)_4^{2+}$  ions to adsorb on the  $c$ -plane top facets of ZnO NWs despite repulsive electrostatic interactions, yielding the significant incorporation of Cu. At the highest pH value, additional attractive electrostatic interactions between the  $\text{Cu}(\text{NH}_3)_4^{2+}$  ion complexes and negatively charged  $c$ -plane top facets further

enhance the incorporation of Cu into ZnO NWs. The present findings provide a deep insight into the physicochemical processes at work during the CBD of ZnO NWs following the addition of copper nitrate, as well as a detailed analysis of the incorporation mechanisms of Cu into ZnO NWs, which are considered beyond the only electrostatic forces usually driving the incorporation of dopants such as Al and Ga.

# 1. INTRODUCTION

The growth of ZnO nanowires (NWs) by chemical bath deposition (CBD) has received increasing interest over the past two decades as a low-cost, low-temperature process that is further compatible with the fabrication of many devices in the fields of piezoelectricity,<sup>1</sup> optoelectronics,<sup>2,3</sup> photovoltaics,<sup>4</sup> detection and sensing.<sup>5</sup> Many efforts have been devoted to controlling the morphology of ZnO NWs by optimizing the structural properties of polycrystalline ZnO and Au seed layers and by tailoring the CBD conditions.<sup>6</sup> In addition to the zinc salt and hexamethylenetetramine (HMTA) typically used as a source of Zn(II) species and HO<sup>-</sup> ions,<sup>7</sup> respectively, chemical additives including polyethylenimine,<sup>8</sup> ethylenediamine,<sup>9</sup> chlorine and citrate ions,<sup>10,11</sup> have also been used to control the aspect ratio of ZnO NWs.

An additional critical issue that has not been investigated in much detail is related to the optimization and control of the electronic structure properties of ZnO NWs grown by CBD, which directly drive their optical and electrical properties. Yet, these properties have a decisive effect on the performances of the related nanoscale devices. In contrast to vapor phase deposition techniques in which the doping of ZnO NWs operates in relative vacuum, the doping of ZnO NWs grown by CBD takes place in an aqueous solution. The present medium involves a large number of forces operating between the growing solid surface and chemical species in the bath, typically electrostatic and chemical forces. Following the work of Joo *et al.*,<sup>12</sup> a recent strategy has optimized the CBD conditions to incorporate the dopants introduced as chemical additives in the bath into the center of ZnO NWs through the adjustment of electrostatic forces.<sup>13-15</sup> The physicochemical processes in the aqueous solution favoring the incorporation of dopants in the lattice benefit from the attractive electrostatic forces between the ion complexes containing the dopants and charged surfaces of ZnO NWs. The present strategy based on the adjustment of electrostatic forces has deeply been investigated in the cases of Al and Ga dopants as two shallow donors in ZnO NWs by adding aluminum nitrate (Al(NO<sub>3</sub>)<sub>3</sub>) and gallium nitrate (Ga(NO<sub>3</sub>)<sub>3</sub>) in the bath, respectively.<sup>13-15</sup> It has been found that the pH value is an important parameter to control as it governs the nature of ion complexes containing the dopants and the sign of the surface charge of ZnO NWs through the magnitude of ζ-potential relative to the isoelectric point.<sup>16</sup> In the narrow initial pH (pH<sub>0</sub>) range of 10.3-11.0, Al(OH)<sub>4</sub><sup>-</sup> and Ga(OH)<sub>4</sub><sup>-</sup> ion complexes adsorb on the positively charged *m*-plane sidewalls of ZnO NWs and hence act as capping agents, resulting in the tunable morphology of ZnO NWs and in the incorporation of Al- and Ga-related defects in the lattice.<sup>13-15</sup> Also, a postdeposition thermal treatment is required to activate the Al doping, in contrast to the Ga doping already activated

in the as-grown ZnO NWs. The present incorporation of Al and Ga dopants as shallow donors drastically increases the density of free electrons in ZnO NWs to boost their electrical conductivity.

While ZnO NWs usually require to be highly conductive for their integration into optoelectronic and photovoltaic applications,<sup>2-4</sup> they should instead be as resistive as possible for piezoelectric devices<sup>1</sup> to reduce the screening of the piezoelectric potential generated under mechanical stress, which basically originates from the high density of free electrons.<sup>17</sup> The need for developing both highly *n*-type doped and intrinsic ZnO NWs through the introduction of shallow donors and compensating acceptors, respectively, has thus appeared as a crucial issue in the field. Among the I-A and I-B group elements in ZnO,<sup>18</sup> copper (Cu) as an abundant element appears as a promising candidate. It has been shown from *ab initio* calculations that Cu preferentially substitutes for zinc sites to form Cu<sub>Zn</sub> with a low formation energy and a corresponding acceptor energy level located in the range of 0.7–1 eV above the valence band maximum.<sup>19,20</sup> Qiu *et al.* also revealed that Cu is able to form shallow donor states by occupying interstitial sites as Cu<sub>i</sub>.<sup>21</sup> However, the chemistry of Cu in aqueous solutions is highly distinct from the chemistry of Al and Ga. An in-depth investigation of the physicochemical processes is thus required for optimizing the Cu incorporation and doping of ZnO NWs grown by CBD. A couple of previous investigations have reported some experimental evidence of the incorporation of Cu into ZnO NWs and nanoparticles grown by CBD by generally adding copper nitrate (Cu(NO<sub>3</sub>)<sub>2</sub>) in the bath.<sup>22-27</sup> Other investigations have reported the use of copper chloride, copper acetate, and copper sulfate.<sup>28-30</sup> However, the required conditions in the chemical bath for inducing the Cu incorporation and the nature of the related mechanisms have not been described in detail. Surprisingly, the influence of the pH in the chemical bath has typically not been considered thoroughly. Additionally, a couple of discrepancies have been found on the possible incorporation sites of Cu in the ZnO lattice. Some authors have reported a decrease in the *c*-lattice parameter of ZnO NWs when the concentration of Cu species in the bath was increased.<sup>22,24,26,28,30</sup> This could be attributed to the presence of Cu<sup>2+</sup><sub>Zn</sub> ions having a smaller ionic radius (0.57 Å) than Zn<sup>2+</sup> ions (0.60 Å) in the fourfold coordinated configuration.<sup>31</sup> Conversely, other authors have reported an increase in the *c*-lattice parameter of ZnO NWs when the concentration of Cu species in the bath was increased.<sup>25,27,29</sup> This could be ascribed to the presence of Cu<sub>i</sub>. Moreover, the incorporated Cu atoms can exhibit either +1<sup>27,28,32-34</sup> or +2<sup>33,35-38</sup> oxidation states, depending on the experimental conditions and the growth method used for ZnO. In the specific case of ZnO NWs grown by CBD, the oxidation state of Cu within the ZnO lattice is still unclear. Additionally, the incorporation of Cu into ZnO NWs has often been associated with a strong increase

in their diameter, suggesting efficient electrostatic interactions between the Cu(II) ions in the bath and ZnO NW facets.<sup>24-27</sup>

In the present article, we perform the growth of ZnO NWs by CBD on top of Au seed layers with a constant  $[\text{Cu}(\text{NO}_3)_2]/[\text{Zn}(\text{NO}_3)_2]$  ratio of 5 %. To elucidate the effects of  $\text{pH}_0$  on the Cu incorporation in the as-grown ZnO NWs, it is systematically varied over a broad range of 6.9-10.9. The morphological properties of ZnO NWs are investigated by field-emission scanning electron microscopy (FESEM) and X-ray diffraction (XRD) measurements, while the behaviors of Zn(II) and Cu(II) species during CBD are assessed through thermodynamic computations. Moreover, the Cu incorporation into ZnO NWs is characterized by energy-dispersive X-ray spectroscopy (EDS), X-ray photoelectron spectroscopy (XPS), and temperature-dependent Raman scattering. These findings provide a deep understanding of the physicochemical processes at work during the CBD of ZnO NWs using  $\text{Cu}(\text{NO}_3)_2$  as an additive, which should be taken into account to achieve Cu-doped ZnO NWs.

## 2. EXPERIMENTAL SECTION

**2.1. Deposition Techniques.** Silicon(100) wafers acting as substrates were dipped for 1 min in a buffered hydrofluoric acid solution followed by a deionized water rinsing, resulting in the removal of the native silicon oxide layer. To ensure the adhesion of Au on the silicon wafers, 10 nm-thick Ti layers were, in a first step, deposited by vacuum evaporation at a rate of  $0.1 \text{ nm}\cdot\text{s}^{-1}$ . In a second step, 10 nm-thick Au seed layers were deposited at a rate of  $0.25 \text{ nm}\cdot\text{s}^{-1}$ . ZnO NWs were synthesized by CBD, in which the samples were immersed face down in reactors sealed with a piece of glass coated with Parafilm, and containing equimolar concentrations of 30 mM of zinc nitrate hexahydrate ( $\text{Zn}(\text{NO}_3)_2\cdot 6\text{H}_2\text{O}$ , Sigma-Aldrich) and hexamethylenetetramine (HMTA,  $\text{C}_6\text{H}_{12}\text{N}_4$ , Sigma-Aldrich) in deionized water. No stirring was performed to favor diffusion processes during the CBD. To reach a constant  $\text{Cu}(\text{NO}_3)_2/\text{Zn}(\text{NO}_3)_2$  ratio of 5 %, 1.5 mM copper nitrate semi(pentahydrate) ( $\text{Cu}(\text{NO}_3)_2\cdot 2.5\text{H}_2\text{O}$ , Sigma-Aldrich) was added to the bath. The initial pH of the solution before heating, denoted as  $\text{pH}_0$ , was changed from 6.9 to 10.9 by further adding ammonia ( $\text{NH}_3$ , Sigma-Aldrich) to the bath with different concentrations ranging from 0 to 1000 mM, as summarized in **Table 1**. The sealed reactors were placed in a regular oven heated at  $85 \text{ }^\circ\text{C}$  for 3 h.

[Cu(NO <sub>3</sub> ) <sub>2</sub> ] / [Zn(NO <sub>3</sub> ) <sub>2</sub> ]	[NH <sub>3</sub> ] added (mM)	pH <sub>0</sub>
0 %	0	6.9
0 %	600	10.7
5 %	0	6.9
5 %	10	7.1
5 %	20	7.2
5 %	350	10.1
5 %	600	10.7
5 %	1000	10.9

**Table 1.** Conditions used during the CBD of ZnO NWs for the series of samples studied, with the corresponding values of pH<sub>0</sub> measured.

**2.2. Characterization Techniques.** The pH during CBD was measured in an *in situ* manner with an InLab Versatile Pro pH electrode from Mettler Toledo. The morphological properties of ZnO NWs were investigated by FESEM images using an FEI Quanta 250 field-emission-gun scanning electron microscope. FESEM-EDS spectra were recorded on ZnO NW arrays using a Bruker X-ray detector incorporated in the FEI Quanta 250 field-emission-gun scanning electron microscope operating at 15 kV. XRD patterns were collected with a Bruker D8 Advance diffractometer using Cu K $\alpha$  radiation ( $\lambda = 0.15406$  nm) according to the Bragg–Brentano configuration. The instrumental shift was corrected by aligning the Si(400) diffraction peak to its theoretical value of 69.132 °. The ZnO, Cu<sub>2</sub>O, and CuO diffraction peaks were indexed according to the ICDD 00-036-1451, 00-005-0667, and 00-048-1548 files, respectively. XPS analyses were performed on a customized Thermo Fisher Scientific Theta 300 system with ultrahigh vacuum conditions ( $<1 \times 10^{-8}$  Pa) equipped with an X-ray source using a monochromatic aluminum anode (1486.6 eV). The recorded spectra were systematically referenced with the 1s neutral carbon peak at 284.8 eV. Raman scattering spectra were recorded using a Horiba/Jobin Yvon Labram spectrometer equipped with a liquid-nitrogen-cooled CCD detector. The 488 nm excitation line of an Ar<sup>+</sup> laser was used with a power on the sample surface lower than 1 mW. The laser beam was focused on a spot size of 1  $\mu\text{m}^2$  using a 50 times long working distance objective. The calibration of the spectra in wavenumber was performed by using a silicon reference sample and considering that the theoretical position of the silicon Raman line is set to 520.7  $\text{cm}^{-1}$ . *In situ* postdeposition annealing was performed under an oxygen atmosphere

from room temperature to 300 °C. The temperature was controlled using a Linkam THMS600 heating stage placed under the Raman microscope.

**2.3. Thermodynamic Computations.** Thermodynamic simulations were performed using Visual MINTEQ software to determine the speciation diagrams of Zn(II) and Cu(II) species as well as the theoretical solubility plots of ZnO and CuO at 85 °C as a function of pH. The two single metallic cations in the aqueous solution (*i.e.*, Zn<sup>2+</sup> and Cu<sup>2+</sup> ions) denoted as M<sup>x+</sup> are able to form amine or hydroxide complexes with the two possible ligands (*i.e.*, NH<sub>3</sub> and HO<sup>-</sup>) denoted as L, according to the general reactions  $nM^{x+} + iL \leftrightarrow M_nL_i^{nx+}$ , where M<sub>n</sub>L<sub>i</sub><sup>nx+</sup> is the complex considered, *i* is the coordination number, and *x* is the cation charge. The related stability constants β<sub>*i*</sub><sup>L</sup> associated with each reaction are given by  $\beta_i^L = \frac{[M_nL_i^{nx+}]}{[M^{x+}]^n[L]^i}$ , whose typical values were taken from the NIST database. To calculate the theoretical solubility plots for each growth condition, the solid forms of Zn- and Cu-related oxides and hydroxides were considered (see **Table S1**).

### 3. RESULTS AND DISCUSSION

**3.1. Effects of the pH<sub>0</sub> of the Solution and the Presence of Cu(NO<sub>3</sub>)<sub>2</sub> in the Chemical Bath on the Growth Mechanisms of ZnO Nanowires.** ZnO NWs were grown on polycrystalline 10 nm-thick Au seed layers composed of (111)-oriented grains. The use of a Au seed layer is highly desirable to form a Schottky contact with ZnO NWs in piezotronic and piezoelectric devices.<sup>39,40</sup> The nucleation of ZnO NWs is typically performed through the heteroepitaxy on top of the (111) Au facets on the grains with the same orientation to form a primary population with a highly vertical alignment.<sup>41</sup> ZnO NWs can also nucleate on (211) facets of the (111) Au grains to form a secondary population of ZnO NWs with a mean tilt angle of around 20 ° with respect to the normal to the substrate surface. The role of Ti and Au in the doping of ZnO NWs is ruled out by the conditions of the chemical bath (*e.g.*, low temperature), which are not appropriate to dissociate the metallic seed layer. The structural morphology of ZnO NWs grown by CBD with Cu(NO<sub>3</sub>)<sub>2</sub>/Zn(NO<sub>3</sub>)<sub>2</sub> ratios of 0 and 5 % and pH<sub>0</sub> values in the range of 6.9–10.9 is presented in **Figure 1** by FESEM imaging. The typical dimensions (*i.e.*, length, diameter, apparent density) of a large number of ZnO NWs were systematically measured from such FESEM images, from which their aspect ratio and deposited volume were deduced. The evolution of these morphological properties with the pH<sub>0</sub> of the solution is summarized in **Figure 2**.

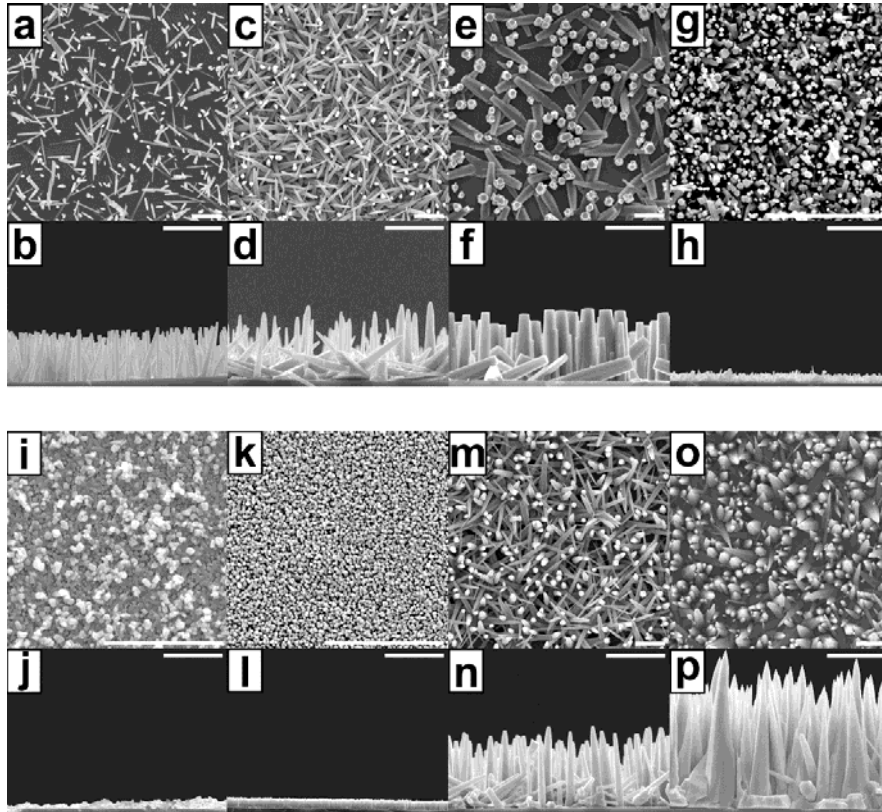


**Figure 1.** Top-view and cross-sectional view FESEM images of ZnO NWs grown by CBD at 85 °C for 3 h with 30 mM  $\text{Zn}(\text{NO}_3)_2$  and HMTA; (a-d)  $\text{Cu}(\text{NO}_3)_2/\text{Zn}(\text{NO}_3)_2$  ratio of 0 % at  $\text{pH}_0$  values of (a,b) 6.9 and (c,d) 10.7, respectively; and (e-p)  $\text{Cu}(\text{NO}_3)_2/\text{Zn}(\text{NO}_3)_2$  ratio of 5 % at  $\text{pH}_0$  values of (e,f) 6.9, (g,h) 7.1, (i,j) 7.2, (k,l) 10.1, (m,n) 10.7, and (o,p) 10.9, respectively. The scale bar is 3  $\mu\text{m}$ .

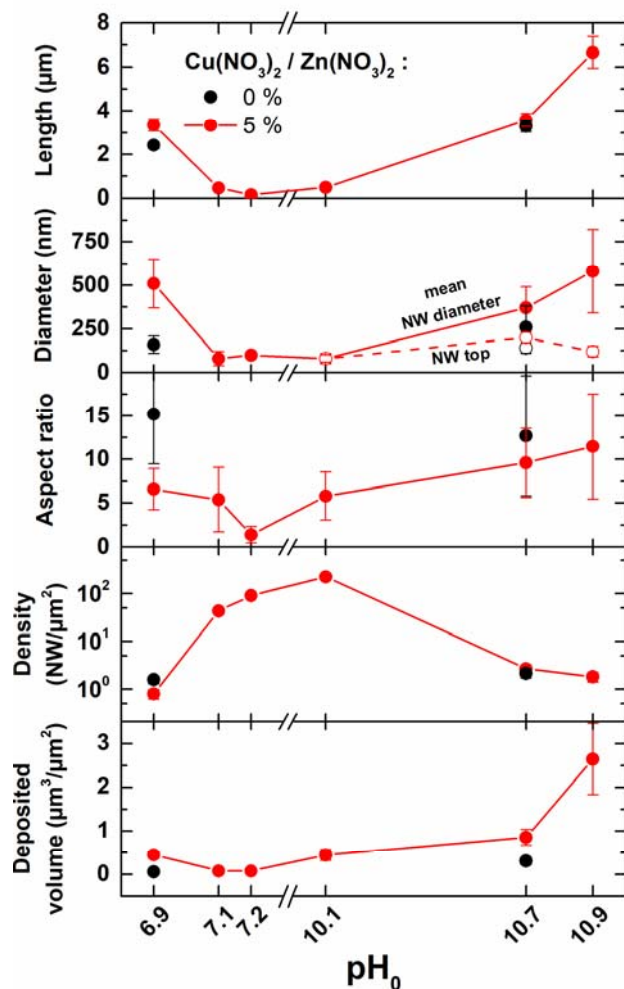


**Figure 2.** Evolutions of the mean length, diameter, aspect ratio, apparent density, and deposited volume of ZnO NWs as a function of the  $\text{pH}_0$ .

As the  $\text{Cu}(\text{NO}_3)_2/\text{Zn}(\text{NO}_3)_2$  ratio is increased from 0 to 5% while setting the  $\text{pH}_0$  to a value of 6.9, a significant increase in the mean length of ZnO NWs from  $2.4 \pm 0.2$  to  $3.4 \pm 0.3 \mu\text{m}$  is revealed as well as an even stronger increase in their mean diameter from  $160 \pm 50$  to  $510 \pm 140 \text{ nm}$ . These dimensional changes are consistent with refs <sup>24-27</sup>. The number density of ZnO NWs correlatively decreases from  $1.6 \pm 0.3$  to  $0.8 \pm 0.2 \text{ NW}/\mu\text{m}^2$ . This indicates that Cu(II) species play a significant role in the growth of ZnO NWs. This could arise from the competition of Zn(II) and Cu(II) species at the nucleation sites on the Au seed layers and at the incorporation sites on the top facets of ZnO NWs.<sup>24,25</sup> As the  $\text{pH}_0$  is increased up to a value of 7.2, the shape of ZnO NWs progressively turns into nanoparticles, as their mean length and diameter decrease to  $0.14 \pm 0.04 \mu\text{m}$  and  $100 \pm 20 \text{ nm}$ , respectively. The number density correlatively increases from  $0.8 \pm 0.2$  to  $91 \pm 10 \text{ NW}/\mu\text{m}^2$ . As a consequence, the aspect ratio of the NWs and the deposited volume both decrease from  $6.6 \pm 2.4$  to  $1.4 \pm 1.0$  and from  $0.45 \pm 0.08$  to  $0.08 \pm 0.02$

$\mu\text{m}^3/\mu\text{m}^2$ , respectively. For  $\text{pH}_0$  values in the range of 7.2–10.1, the heterogeneous growth from the substrate becomes negligible and a very small amount of ZnO is deposited. As the  $\text{pH}_0$  value is further increased from 10.1 to 10.9, the mean length, diameter, aspect ratio, and deposited volume of ZnO NWs greatly increase up to  $6.7 \pm 0.7 \mu\text{m}$ ,  $580 \pm 240 \text{ nm}$ ,  $11.5 \pm 6.0$ , and  $2.6 \pm 0.8 \mu\text{m}^3/\mu\text{m}^2$ , respectively. Correlatively, their number density decreases to  $1.8 \pm 0.4 \text{ NW}/\mu\text{m}^2$  owing to coalescence effects. The formation of pencil-shaped NWs is additionally shown, which could be attributed to the erosion of the NW top facets by  $\text{HO}^-$  ions, as suggested by Willander *et al.*<sup>42</sup> This feature could be further enhanced by the drastic increase in the growth rate along the polar  $c$ -axis occurring in this range of  $\text{pH}_0$  values, preventing the complete formation of the surface  $m$ -planes on their sidewalls.

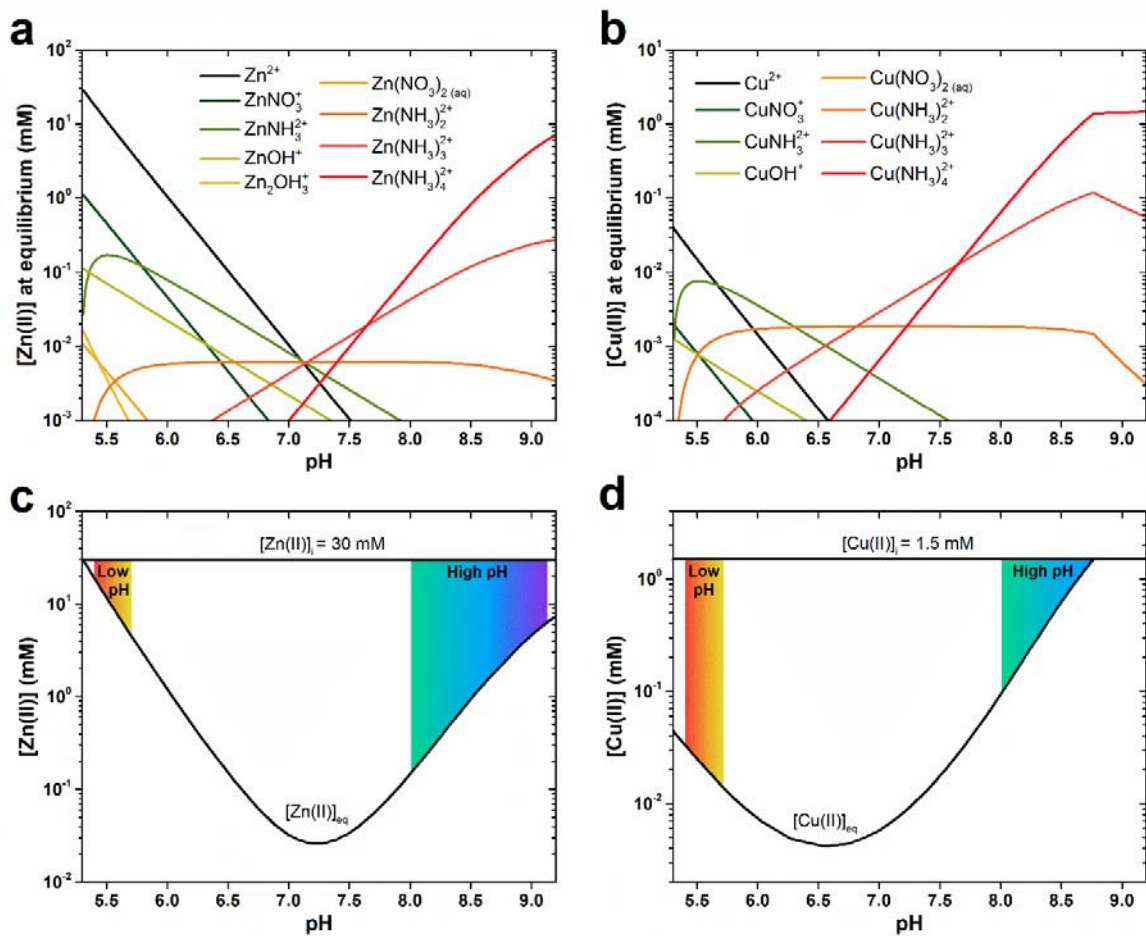


**Figure 3.** Speciation diagrams of (a) Zn(II) and (b) Cu(II) species and theoretical solubility plots of (c) Zn(II) and (d) Cu(II) species at 85 °C as a function of pH, as computed by Visual MINTEQ software. The initial concentrations of  $\text{Zn}^{2+}$  and  $\text{Cu}^{2+}$  ions were set to 30 and 1.5 mM, respectively, and the  $\text{NH}_4^+$  concentration was varied up to 1200 mM. The supersaturation ranges of both Zn(II) and Cu(II) species are illustrated by the colored areas on the theoretical solubility plots and were estimated by the difference between the initial concentrations of  $\text{Zn}^{2+}$  and  $\text{Cu}^{2+}$  ions and the equilibrium concentrations of soluble Zn(II) and Cu(II) species, respectively. The low-pH region

corresponds to the samples with  $\text{pH}_0$  values in the range of 6.9-7.2, while the high-pH region corresponds to the samples with  $\text{pH}_0$  values in the range of 10.1-10.9.

To thoroughly understand the morphological evolution of ZnO NWs with the  $\text{pH}_0$  in the presence of  $\text{Cu}(\text{NO}_3)_2$  in the chemical bath, thermodynamical computations were carried out using Visual MINTEQ software. Speciation diagrams and theoretical solubility plots were calculated for Zn(II) and Cu(II) species, respectively, as presented in **Figure 3**. The computations were performed by varying the concentration of  $\text{NH}_4^+$  up to 1200 mM while fixing the temperature to 85 °C and the initial concentrations of  $\text{Zn}^{2+}$  and  $\text{Cu}^{2+}$  ions to 30 and 1.5 mM, respectively. The corresponding pH values were calculated from the mass and charge balance in the software. Additionally, to assess the evolution of the pH during the growth of ZnO NWs, *in situ* pH measurements were performed for each sample of the series, as presented in **Figure S1**. After an initial decrease of the pH occurring in the first 45 min of the ZnO NW growth due to the thermalization of the bath up to 85 °C, the pH values are roughly stable, readily extracted, and correspond to the steady-state pH. Accordingly, the steady-state pH stabilizes around 5.4–5.7 and 8.0–9.1 as the  $\text{pH}_0$  of the solution starts in the ranges of 6.9–7.2 and 10.1–10.9, respectively. These two steady-state pH ranges are defined as the low- and high-pH regions, respectively. From the theoretical solubility plots in **Figures 3c,d**, the supersaturation related to ZnO and CuO precipitations can be deduced and are represented as colored areas on the graphs for both low- and high-pH regions. From **Figures 3a,c**, three regimes can be identified for the growth of ZnO NWs : (i) in the low-pH region, Zn(II) species mainly form  $\text{Zn}^{2+}$  ions while the supersaturation strongly increases with the pH, which progressively favors the homogeneous growth in the bath at the expense of the heterogeneous growth on top of the Au seed layer, (ii) for intermediate pH values in the range of 5.7-8.0, the supersaturation is very high, resulting in the negligible heterogeneous growth and very few Zn(II) ions remaining in the bath, (iii) in the-high pH region, Zn(II) species predominantly form  $\text{Zn}(\text{NH}_3)_4^{2+}$  ion complexes, reducing the supersaturation by further increasing the pH and thus strongly increasing the growth rate of ZnO NWs. The strong morphological variations of ZnO NWs with the  $\text{pH}_0$  value are thus basically explained by the corresponding variations in supersaturation, as already reported in previous studies.<sup>13,15,43</sup> Interestingly, from **Figures 3b,d**, we can see that Cu(II) species follow similar behavior as they mainly form  $\text{Cu}^{2+}$  ions in the low-pH region and  $\text{Cu}(\text{NH}_3)_4^{2+}$  ion complexes in the high-pH region. This strongly contrasts with the behavior of Al(III) and Ga(III) species in the aqueous solution reported in previous studies, as they typically form neutral  $\text{X}(\text{OH})_3$  complexes (with  $\text{X} = \text{Al}$  or  $\text{Ga}$ ) in the low-pH region and negatively charged  $\text{X}(\text{OH})_4^-$  complexes in the high-pH region.<sup>13,15</sup> The

formation of  $\text{Al}^{3+}$  and  $\text{Ga}^{3+}$  ions is favored in a lower pH range, where the growth of ZnO NWs by CBD is hampered. The positively charged Cu(II) species formed in the present case for both low- and high-pH regions indicate the occurrence of different electrostatic interactions at work with ZnO NW facets as compared to the cases of Al or Ga. This in turn could lead to different incorporation mechanisms of Cu atoms. Additionally, the supersaturation of Cu(II) species is very high in the low-pH region, and progressively decreases until being negligible in the high-pH region. This suggests that massive precipitation of CuO is thermodynamically favorable during the growth of ZnO NWs with a  $\text{pH}_0$  value in the range of 6.9–7.2 while a large majority of Cu(II) species remain soluble in the form of  $\text{Cu}(\text{NH}_3)_4^{2+}$  complexes as the  $\text{pH}_0$  value lies in the range of 10.1–10.9.

To fully elucidate the behavior of Cu atoms introduced in the chemical bath, several structural and chemical analyses were carried out on the series of samples. The presence of Cu was first assessed by FESEM-EDS measurements, where all of the spectra were recorded under identical conditions. They were further normalized with respect to the Zn  $\text{K}_\alpha$  line pointed at 8.63 keV, as presented in **Figure 4**.

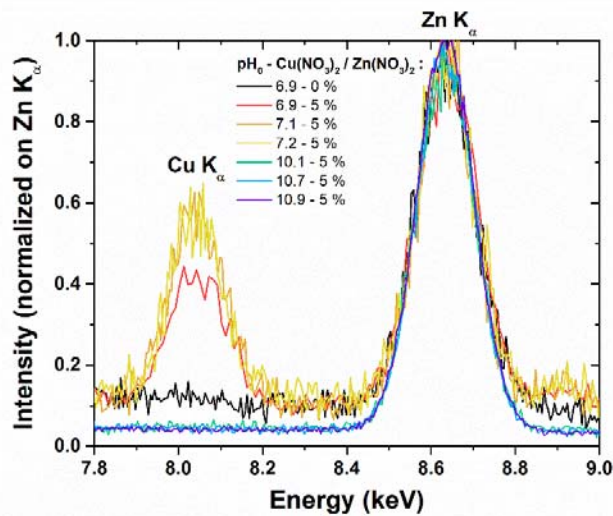


**Figure 4.** FESEM-EDS spectra of ZnO NWs grown at  $\text{pH}_0$  values in the range of 6.9–10.9 and with a  $\text{Cu}(\text{NO}_3)_2/\text{Zn}(\text{NO}_3)_2$  ratio of 0 or 5 %. All of the spectra were normalized with respect to the Zn  $\text{K}_\alpha$  line pointed at 8.63 keV.

In the energy range from 7.8 to 9.0 keV, a strong peak pointed at 8.04 keV and assigned to the Cu  $\text{K}_\alpha$  line occurs as the  $\text{pH}_0$  value lies in the range of 6.9–7.2. In contrast, this peak is absolutely not observed in the deposits grown at higher  $\text{pH}_0$  values in the range of 10.1–10.9. This indicates that Cu is massively present for the samples with  $\text{pH}_0$  values in the range of 6.9–7.2, while the other samples have the Cu content at least below the detection limit of the apparatus ( $< 0.2$  atom % Cu). The structural composition of the deposits was determined from the XRD

patterns in **Figure 5a**, where several diffraction peaks attributed to the wurtzite structure of ZnO are revealed. The ZnO NWs are typically oriented in the  $\langle 0001 \rangle$  direction (*i.e.*, along the *c*-axis), as shown through the strong intensity of the (0002) diffraction peak at  $34.4^\circ$  observed for all samples. The presence of minor diffraction peaks attributed to other directions of ZnO, as well as their variable level of intensities from one sample to another, are attributed to the drastic changes of the verticality and deposited volume of ZnO NWs within the series of samples. Interestingly, the sample with a  $\text{pH}_0$  value of 6.9 and a  $\text{Cu}(\text{NO}_3)_2/\text{Zn}(\text{NO}_3)_2$  ratio of 5 % shows an additional diffraction peak at  $36.4^\circ$ , which is attributed to the  $Pn\bar{3}m$  cubic structure of  $\text{Cu}_2\text{O}$  through the (111) reflection. In contrast, the sample with a  $\text{pH}_0$  value of 7.1 shows three additional diffraction peaks at  $32.6$ ,  $35.4$ , and  $61.4^\circ$ , which are all attributed to the  $C2/c$  monoclinic structure of CuO through the (110), (002)/(-111), and (-113) reflections. Similarly, the sample with a  $\text{pH}_0$  value of 7.2 shows one additional diffraction peak at  $35.4^\circ$ , which is also attributed to the  $C2/c$  monoclinic structure of CuO through the (002)/(-111) reflections. This unambiguously shows the presence of a crystalline copper oxide phase formed on top of the Au seed layers, which can crystallize into either  $\text{Cu}_2\text{O}$  at a  $\text{pH}_0$  value of 6.9, or CuO at a  $\text{pH}_0$  value in the range of 7.1–7.2. The present statement is consistent with both the high Cu content observed by FESEM-EDS measurements in **Figure 4**, and the massive CuO precipitation predicted in this range of pH by thermodynamic computations in **Figure 3d**. The formation of these copper oxide phases in the presence of  $\text{Cu}(\text{NO}_3)_2$  also contrasts strongly with the absence of aluminum oxide and gallium oxide phases in the presence of  $\text{Al}(\text{NO}_3)_3$  and  $\text{Ga}(\text{NO}_3)_3$ .<sup>13–15</sup> The reaction kinetics to form the copper oxide phases are certainly favorable in the present case. The formation of a copper oxide phase is further confirmed by high-magnification FESEM images of the samples with  $\text{pH}_0$  values of 6.9, 7.1, and 7.2, as presented in **Figure 5b-d**, respectively. In addition to ZnO NWs exhibiting hexagonal facets, the presence of nanoplatelets clearly occurs and can be attributed to the formation of copper oxide nanocrystals. Although the precipitation of  $\text{Cu}_2\text{O}$  at a  $\text{pH}_0$  value of 6.9 was not predicted by thermodynamic computations, Terasako et al. reported the possibility of tuning the nature of copper oxide films from  $\text{Cu}_2\text{O}$  to CuO by increasing the pH of the solution.<sup>44</sup> Thus, the value of the pH somehow influences the capability of Cu(II) ions, mainly present in the  $\text{Cu}^{2+}$  form in this range of pH, to reduce into Cu(I) ions, presumably in the  $\text{Cu}^+$  form, resulting in the formation of different copper oxide phases.

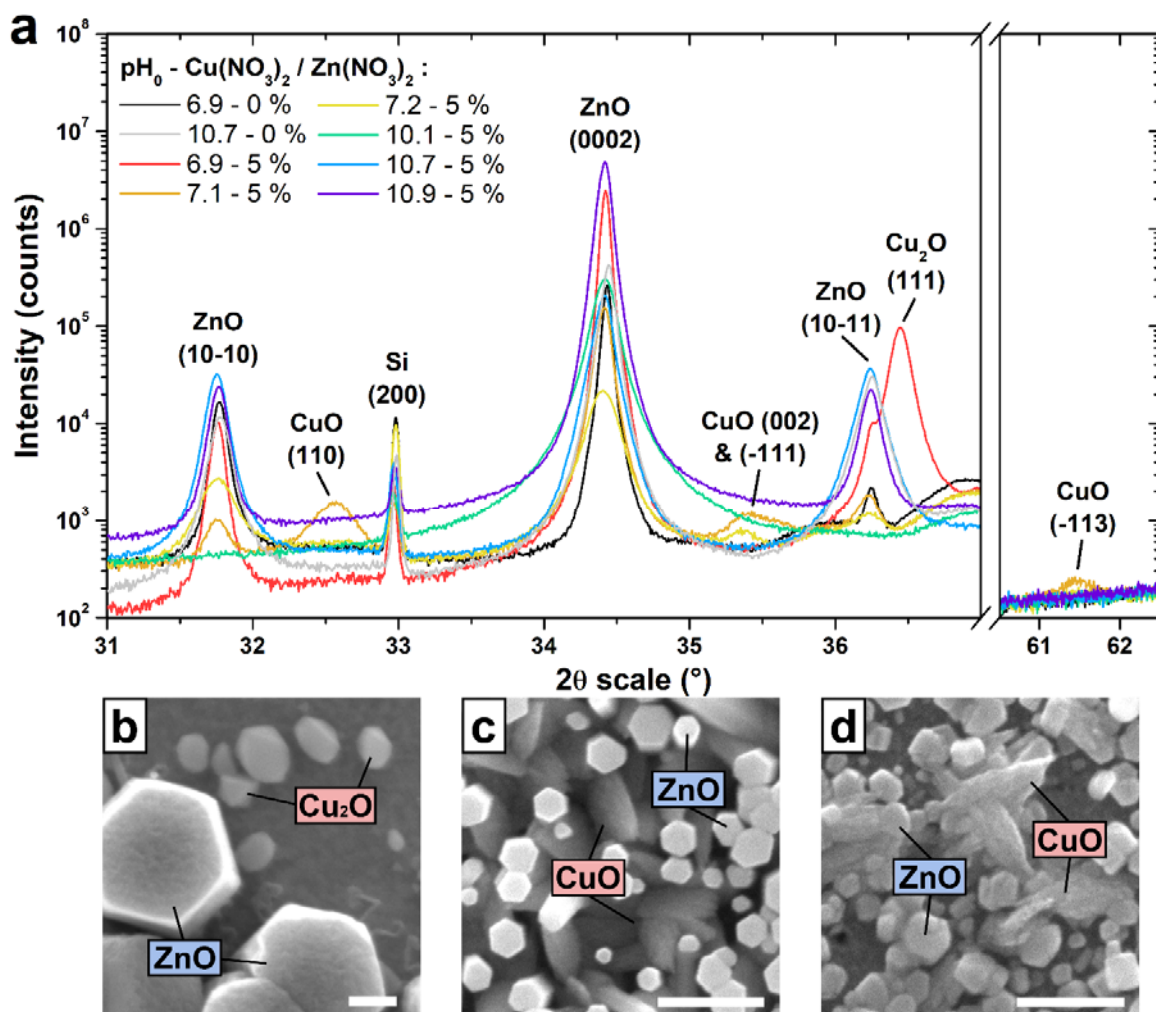


**Figure 5.** (a) XRD patterns of ZnO NWs grown at  $\text{pH}_0$  values in the range of 6.9–10.9 and with a  $\text{Cu}(\text{NO}_3)_2/\text{Zn}(\text{NO}_3)_2$  ratio of 0 or 5 %. (b-d) High-magnification top-view FESEM images of ZnO NWs grown by CBD at 85 °C for 3 h with 30 mM  $\text{Zn}(\text{NO}_3)_2$  and HMTA, with a  $\text{Cu}(\text{NO}_3)_2/\text{Zn}(\text{NO}_3)_2$  ratio of 5 % and at  $\text{pH}_0$  values of (b) 6.9, (c) 7.1, and (d) 7.2. Typical ZnO,  $\text{Cu}_2\text{O}$ , and CuO crystals are pointed out. The scale bar is 300 nm.

### 3.2. Effects of the $\text{pH}_0$ of the Solution and of the Presence of $\text{Cu}(\text{NO}_3)_2$ in the Chemical Bath on the Incorporation of Copper into ZnO Nanowires.

To get more insight into the possible incorporation of Cu atoms in ZnO NWs, the position of the ZnO (0004) diffraction peak was carefully measured for each sample from the XRD patterns in **Figure 6a**, and compared to its theoretical value of 72.56 °, as presented in **Figure 6b**. A slight shift toward lower angles (from 0.01 to 0.05 °) is noticed for the samples with  $\text{pH}_0$  values of 7.1, 7.2, and 10.9, suggesting a larger ZnO lattice parameter in the  $c$ -axis of the wurtzite structure. In contrast, the peak position of the samples with other pH values is roughly in agreement with the theoretical value. A larger  $c$ -lattice parameter of ZnO in the context of Cu incorporation is in agreement with refs. <sup>25,27</sup> and is usually associated with the presence of Cu in interstitial sites of the lattice. Moreover, no epitaxial strain is expected to occur in the

ZnO lattice, as the stress created during the heteroepitaxy of the NWs on Au grains is known to be completely relieved through the creation of extended defects including misfit dislocations.<sup>41</sup> Surface stress-induced strain can be further neglected in the range of diameters considered.<sup>45</sup> In the absence of dopant incorporation, the residual strain in bare ZnO NWs grown by CBD with a diameter larger than 50 nm is roughly zero.<sup>46</sup> Thus, the present result indicates that Cu atoms were successfully incorporated for the samples with pH<sub>0</sub> values of 7.1, 7.2, and 10.9. The presence of residual impurities or intentional dopants in the ZnO crystal is commonly correlated with the creation of defects in the lattice. They can be detected through Raman spectroscopy by the occurrence of additional modes (AMs) specifically for Al, Ga, N, Sb, and Fe,<sup>14,15,47,48</sup> as well as by the change of the shape and position of the E<sub>2</sub> (high) mode related to the wurtzite structure of ZnO.<sup>25,28,34,49,50</sup> For this purpose, Raman spectra of ZnO NWs were recorded at room temperature and are presented in **Figure 7a**. The measurements were performed in the backscattering configuration, where the laser light propagation is perpendicular to the substrate (*i.e.*, parallel to the ZnO NW *c*-axis). The observation of four characteristic Raman lines associated with the wurtzite structure of ZnO is achieved in all of the samples, regardless of the pH<sub>0</sub> values, one of them – A<sub>1</sub> (TO) – being more or less visible for samples containing a very small amount of ZnO (pH<sub>0</sub> = 7.1, 7.2, 10.1). The Raman lines corresponding to the E<sub>2</sub> (low), A<sub>1</sub> (TO), E<sub>2</sub> (high), and A<sub>1</sub> (LO) modes are located at 100, 380, 439, and 581 cm<sup>-1</sup>, respectively.<sup>51</sup> Additionally, second-order features appear at 331 cm<sup>-1</sup> (E<sub>2</sub> (high) – E<sub>2</sub> (low)) and at 1050–1180 cm<sup>-1</sup>. The sample grown at a pH<sub>0</sub> value of 6.9 and a Cu(NO<sub>3</sub>)<sub>2</sub>/Zn(NO<sub>3</sub>)<sub>2</sub> ratio of 5 % also shows three characteristic Raman lines located at 150, 217 and 647 cm<sup>-1</sup>, which are respectively associated with the T<sub>1u</sub>, 2E<sub>u</sub>, and T<sub>1u</sub> vibration modes of the *Pn* $\bar{3}m$  cubic structure of Cu<sub>2</sub>O,<sup>52</sup> as we could expect from the Cu<sub>2</sub>O nanocrystals evidenced in this sample. Similarly, the samples grown at pH<sub>0</sub> values of 7.1 and 7.2 show three characteristic Raman modes associated with the monoclinic structure of CuO belonging to the *C2/c* space group, which are also expected from the CuO nanocrystals evidenced in these samples. The Raman lines corresponding to the A<sub>g</sub>, B<sub>g</sub><sup>1</sup>, and B<sub>g</sub><sup>2</sup> modes are located at 298, 356, and 628 cm<sup>-1</sup>, respectively.<sup>53</sup> However, the Raman spectra do not exhibit any AMs that could be attributed to the presence of dopant-induced defects in ZnO NWs. This could be expected as the incorporation of Cu is not well known to induce this kind of AMs in ZnO, unlike Al, Ga, N, Sb, and Fe.<sup>47</sup> Moreover, no significant change in the characteristics of the E<sub>2</sub> (high) mode of ZnO has been observed, indicating no change in the crystalline structure quality. **Figure 7b** reveals the temperature-dependent Raman spectra of ZnO NWs grown at a pH<sub>0</sub> value of 10.7 and with a Cu(NO<sub>3</sub>)<sub>2</sub>/Zn(NO<sub>3</sub>)<sub>2</sub> ratio of 5 %. No AM is revealed and no broadening of the E<sub>2</sub> (high) mode

of ZnO is observed when the sample is heated up to 300 °C, suggesting no thermal activation in the present case and that the crystalline structure quality is also maintained with temperature. However, the absence of AMs after annealing in the high-pH region indicates that the incorporation of residual impurities including Al coming from the chemical precursors does not proceed either in the presence of  $\text{Cu}(\text{NO}_3)_2$ .<sup>14,15</sup> Similarly, ZnO NWs grown at  $\text{pH}_0$  values of 7.1 and with a  $\text{Cu}(\text{NO}_3)_2/\text{Zn}(\text{NO}_3)_2$  ratio of 5 % keep as well a high crystalline quality when the sample is heated up to 300 °C. No AM occurs in their corresponding temperature-dependent Raman spectra (**Figure S2**).

XPS spectra, recorded in the Cu 2p energy range as presented in **Figure 8**, also confirm the presence of CuO in the samples with  $\text{pH}_0$  values of 7.1 and 7.2. In addition to the Cu 2p<sub>1/2</sub> and Cu 2p<sub>3/2</sub> peaks pointed at 952.6 and 932.7 eV, respectively, the clear satellite peaks seen at 963.1 eV, and at around 939–943 eV, are attributed to the Cu(II) oxidation state.<sup>54</sup> Similarly, the spectrum corresponding to the sample with a  $\text{pH}_0$  value of 6.9 and a  $\text{Cu}(\text{NO}_3)_2/\text{Zn}(\text{NO}_3)_2$  ratio of 5 % (red curve) confirms the presence of Cu<sub>2</sub>O. Indeed, the Cu 2p<sub>1/2</sub> and Cu 2p<sub>3/2</sub> peaks are shifted to lower energies by a value of 1.3 eV as compared to the samples with  $\text{pH}_0$  values of 7.1 and 7.2 while no satellite peak is observed, indicating the presence of the Cu(I) oxidation state in this sample.<sup>54</sup> Interestingly, these peaks show as well a second contribution aligned with the main features of the samples with  $\text{pH}_0$  values of 7.1 and 7.2 and thus attributed to the Cu(II) oxidation state. These weak contributions are also revealed on the samples with  $\text{pH}_0$  values in the range of 10.1–10.9 where no copper oxide phase was observed, indicating that the incorporation of Cu(II) elements occurs in all of the samples. The quantitative analysis performed on these XPS spectra correlates these qualitative observations, as the presence of copper oxide phases in the samples with  $\text{pH}_0$  values in the range of 6.9–7.2 is associated with high Cu contents in the range of 3–13 atom %, while the presence of the Cu(II) elements in the samples with  $\text{pH}_0$  values in the range of 10.1–10.9 is associated with lower Cu contents below 1 atom %. Additionally, the sample with a  $\text{Cu}(\text{NO}_3)_2/\text{Zn}(\text{NO}_3)_2$  ratio of 0 % and a  $\text{pH}_0$  value of 6.9 (black curve) show small features aligned with the Cu 2p peaks attributed to the Cu(I) oxidation state, indicating that the contamination of Cu(I) elements occurred from the chemical precursors used during CBD. It should be noted here that the present XPS measurements provide data up to approximately 7 nm below the ZnO NW surface. The incorporation of Cu atoms is thus shown in the subsurface of ZnO NWs.

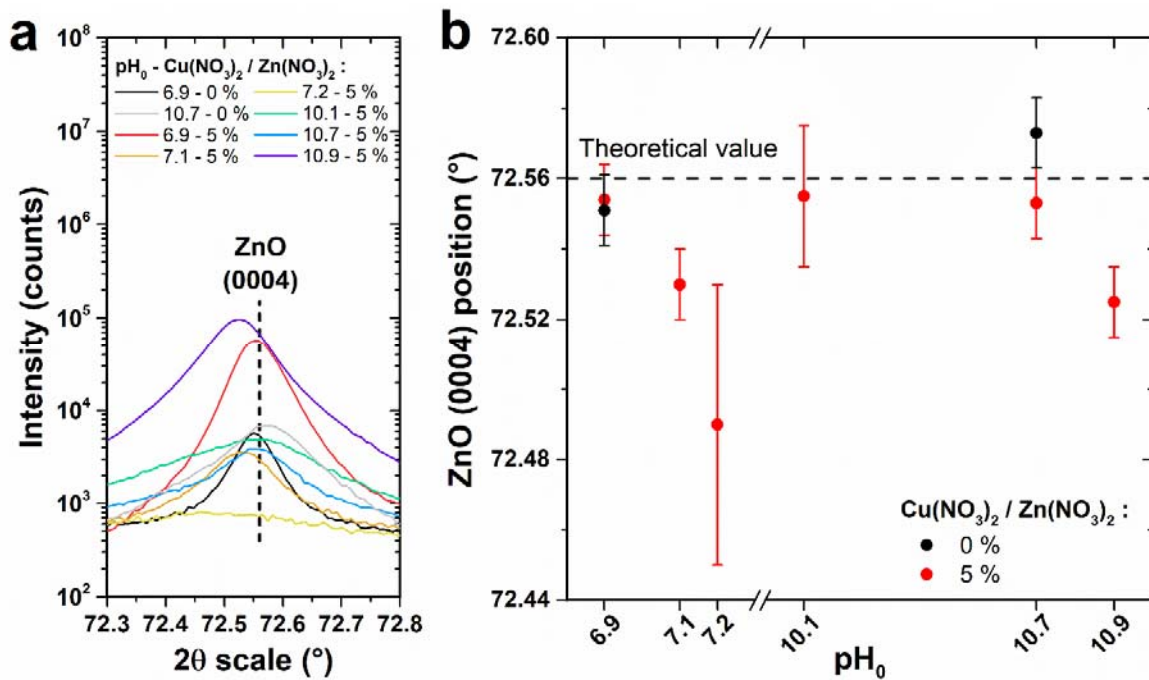


**Figure 6.** (a) XRD patterns centered on the ZnO (0004) diffraction peak of ZnO NWs grown at  $\text{pH}_0$  values in the range of 6.9–10.9 and with a  $\text{Cu}(\text{NO}_3)_2/\text{Zn}(\text{NO}_3)_2$  ratio of 0 or 5 %. (b) Evolution of the position of the (0004) diffraction peak of ZnO with the  $\text{pH}_0$ . The dashed lines in both figures represent the theoretical position of the ZnO (0004) diffraction peak according to the ICDD 00-036-1451 file.

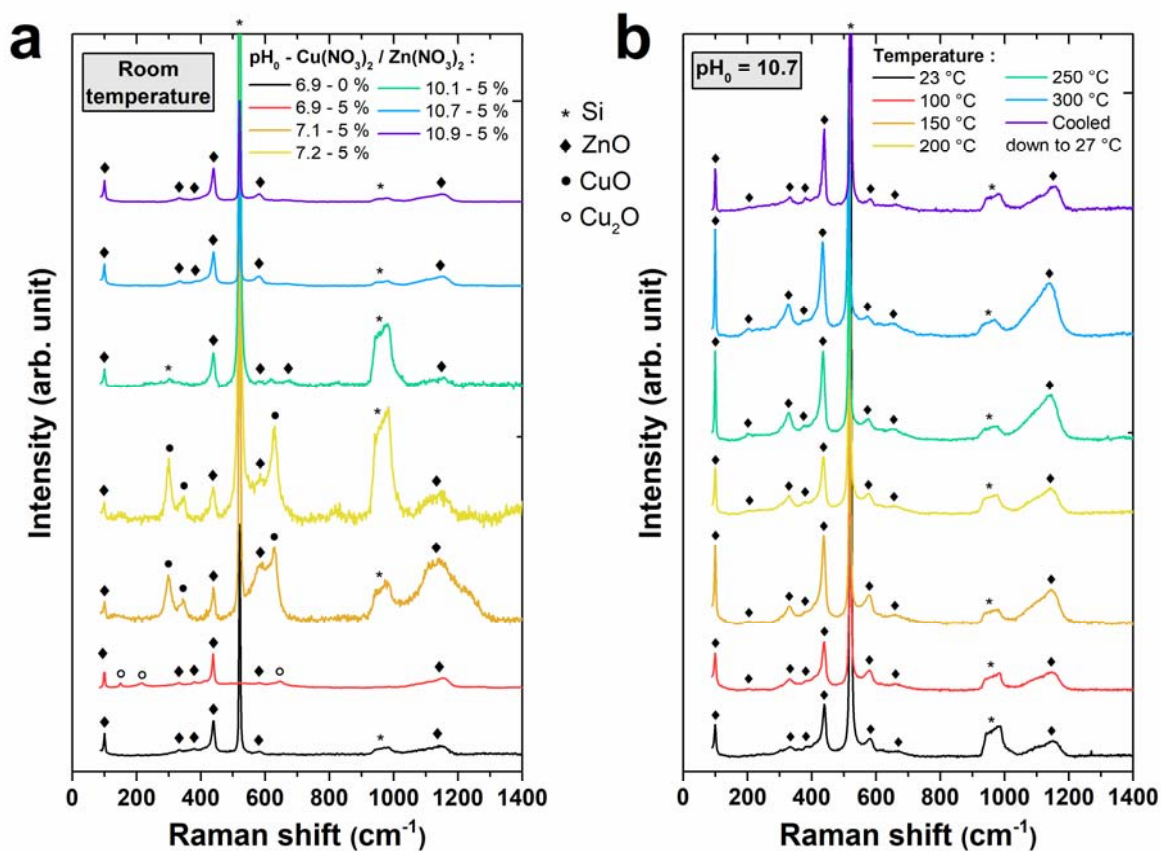


**Figure 7.** (a) Raman spectra of ZnO NWs grown at  $\text{pH}_0$  values in the range of 6.9–10.9 and with a  $\text{Cu}(\text{NO}_3)_2/\text{Zn}(\text{NO}_3)_2$  ratio of 0 or 5 %. All of the spectra were normalized with respect to the  $\text{ZnO E}_2^{\text{high}}$  peak pointed at  $438 \text{ cm}^{-1}$ . (b) Raman spectra of ZnO NWs grown at a  $\text{pH}_0$  value of 10.7 and with a  $\text{Cu}(\text{NO}_3)_2/\text{Zn}(\text{NO}_3)_2$  ratio of 5 %, as collected from room temperature to  $300 \text{ }^\circ\text{C}$  under an oxygen atmosphere.

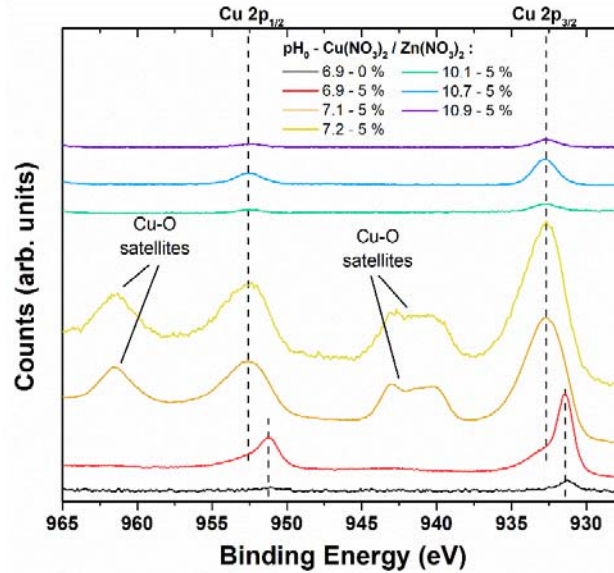


**Figure 8.** XPS spectra centered on the Cu 2p energy range of ZnO NWs grown at  $\text{pH}_0$  values in the range of 6.9–10.9 and with a  $\text{Cu}(\text{NO}_3)_2/\text{Zn}(\text{NO}_3)_2$  ratio of 0 or 5 %.

### 3.3. Physicochemical Processes and Copper Incorporation Mechanisms.

The physicochemical processes following the addition of  $\text{Cu}(\text{NO}_3)_2$  during the CBD of ZnO NWs are summarized in **Figure 9**. The incorporation of Cu as a dopant into the center of ZnO NWs is driven by the adsorption process of Cu(II) species on their growing solid surfaces. The free energy of adsorption of Cu species involves the energetic contributions related to electrostatic forces, solvation forces, and chemical forces.<sup>55,56</sup> With regards to the electrostatic forces, the point-of-zero-charge (PZC) of ZnO, corresponding to the pH value at which a given surface switches from positively to negatively charged, represents a key parameter.<sup>16</sup> It was reported to be equal to  $8.7 \pm 0.2$  and  $10.2 \pm 0.2$  for the polar *c*-plane and nonpolar *m*-plane of ZnO, respectively.<sup>57,58</sup> From the *in situ* pH measurements presented in **Figure S1**, we can infer that the *m*-plane sidewalls remain positively charged in the whole range of pH studied, while the *c*-plane top facets are positively charged up to a  $\text{pH}_0$  value of 10.7 and become negatively charged at a  $\text{pH}_0$  value of 10.9. Depending on the  $\text{pH}_0$  value, the electrostatic forces between the Cu(II) species and growing solid surfaces are thus attractive or repulsive and the magnitude of the electrostatic free energy is drastically altered. In contrast, the solvation free energy systematically acts as an energy barrier for the adsorption of Cu species on the growing solid surfaces. Eventually, the chemical free energy originating from the short-range dispersion forces

and interfacial hydrogen bonding strongly promotes the adsorption process of Cu(II) species on the growing solid surfaces. The balance between the pH-dependent energetic contributions to the free energy of adsorption determines the behavior of Cu(II) species in the bath close to the free surfaces of ZnO NWs.

At a  $\text{pH}_0$  value of 6.9 (**Figure 9a**), the dominant  $\text{Cu}^{2+}$  ions in the bath originating from the solubilization of  $\text{Cu}(\text{NO}_3)_2$  undergo a change of oxidation state from +2 to +1, leading to the formation of  $\text{Cu}^+$  ions. Owing to the large supersaturation of Cu species at that pH, the crystallization of nanocrystals with the  $\text{Cu}_2\text{O}$  phase occurs concomitantly to the growth of ZnO NWs. However, a very small amount of  $\text{Cu}^{2+}$  ions remains in the +2 oxidation state. These  $\text{Cu}^{2+}$  ions preferentially interact with the positively charged *c*-plane top facets of the ZnO NWs and adsorb on these growing solid surfaces despite repulsive electrostatic forces. The chemical free energy of  $\text{Cu}^{2+}$  ions is typically very large on the surfaces of metal oxides<sup>56</sup> and thus overcomes the energy barrier attributed to the small electrostatic free energy related to the +2 oxidation state and to the large solvation free energy coming from the low dielectric constant of ZnO as compared to the one of water. Basically,  $\text{Cu}^{2+}$  ions compete with  $\text{Zn}^{2+}$  ions during the elongation process of ZnO NWs and incorporate into the lattice owing to their similar ionic structures. The amount of incorporated Cu atoms is however very small owing to the very minority  $\text{Cu}^{2+}$  ions available and hence no significant change in the ZnO crystal structure is induced.

When the  $\text{pH}_0$  value lies in the range of 7.1–7.2 (**Figure 9b**), the dominant  $\text{Cu}^{2+}$  ions in the bath originating from the solubilization of  $\text{Cu}(\text{NO}_3)_2$  keep the +2 oxidation state. Owing to the large supersaturation of Cu species in that pH range, the formation of nanocrystals with the CuO phase takes place concomitantly to the growth of ZnO NWs. However, a significant amount of  $\text{Cu}^{2+}$  ions remains soluble in the bath. Similarly to the sample with a  $\text{pH}_0$  value of 6.9, these  $\text{Cu}^{2+}$  ions preferentially interact with the positively charged *c*-plane top facets of the ZnO NWs and adsorb on these growing solid surfaces despite repulsive electrostatic forces. By increasing the pH value close to the PZC,<sup>56</sup> the chemical free energy readily overcomes the smaller electrostatic free energy and the large solvation free energy. As no change of oxidation state occurs in this range of pH, a larger amount of  $\text{Cu}^{2+}$  ions is available to interact with the ZnO NWs, leading to a more significant incorporation of Cu atoms in the ZnO lattice. These Cu atoms are expected to form  $\text{Cu}_{\text{Zn}}$  as acceptors owing to their low formation energy,<sup>19,20</sup> but the presence of nitrogen- and hydrogen-related defects with a high concentration<sup>59,60</sup> may significantly alter the nature of Cu-related defects. However, as the amount of incorporated Cu is very high in this range of pH, a large number of  $\text{Cu}_i$  as donors is also created presumably, affecting the ZnO crystal structure.<sup>29</sup>

When the  $\text{pH}_0$  value lies in the range of 10.1–10.7 (**Figures 9c**), the Cu(II) species are predominant in the form of  $\text{Cu}(\text{NH}_3)_4^{2+}$  ions, and remain soluble in the bath. The low supersaturation of Cu species in that pH range is not favorable for the crystallization of copper oxide phases and hence only ZnO NWs are formed. The  $\text{Cu}(\text{NH}_3)_4^{2+}$  ions preferentially interact with the positively charged *c*-plane top facets of the ZnO NWs despite repulsive electrostatic interactions. On the one hand, the chemical free energy of  $\text{Cu}(\text{NH}_3)_4^{2+}$  ions is much smaller than the one of  $\text{Cu}^{2+}$  ions.<sup>56</sup> On the other hand, it is well known that their related electrostatic and solvation free energies on the surfaces of metal oxides are also much smaller than the ones of  $\text{Cu}^{2+}$  ions, such that their adsorption process is still energetically favorable.<sup>56</sup> In particular, the  $\text{Cu}(\text{NH}_3)_4^{2+}$  ions are likely located on the outer Stern plane, in contrast to the previous  $\text{Cu}^{2+}$  ions penetrating through the Stern plane. Again,  $\text{Cu}(\text{NH}_3)_4^{2+}$  ions compete with  $\text{Zn}(\text{NH}_3)_4^{2+}$  ions during the elongation process of ZnO NWs and incorporate into the lattice owing to their similar ionic structures. In that pH range, the amount of incorporated Cu atoms is nevertheless relatively small despite the large amount of  $\text{Cu}(\text{NH}_3)_4^{2+}$  ions in the bath owing to the small chemical free energy.

At a  $\text{pH}_0$  value of 10.9 (**Figure 9d**), the Cu(II) species follow a similar solubilization process as they predominantly form  $\text{Cu}(\text{NH}_3)_4^{2+}$  ions and no copper oxide phase is formed. However, the pH of the chemical bath is higher than the PZC of the *c*-plane of ZnO, which becomes negatively charged. Thus, the  $\text{Cu}(\text{NH}_3)_4^{2+}$  ions are subject to attractive electrostatic forces with the *c*-plane top facets of ZnO NWs and hence adsorb readily on these growing solid surfaces. The addition of the electrostatic free energy to the chemical free energy largely overcomes the energy barrier attributed to the solvation free energy, such that important incorporation of Cu atoms occurs into the ZnO lattice. Similarly to the samples with  $\text{pH}_0$  values in the range of 7.1–7.2, both  $\text{Cu}_{\text{Zn}}$  as acceptors and  $\text{Cu}_i$  as donors are expected to be created in the lattice owing to the large amount of incorporated Cu, but the presence of nitrogen- and hydrogen-related defects in ZnO NWs may play a role. Besides the present incorporation mechanisms of Cu and its interactions with the *c*-plane top facets of ZnO NWs, other physicochemical processes due to the addition of  $\text{Cu}(\text{NO}_3)_2$  may occur in the bath. In particular, the increase in the NW diameter observed when adding  $\text{Cu}(\text{NO}_3)_2$  into the bath in the low-pH region, as well as the absence of residual impurities in the ZnO NWs when grown in the high-pH region, suggests that Cu(II) species may also interact with the *m*-plane sidewalls of ZnO NWs.

As a consequence, Cu follows very singular incorporation mechanisms in ZnO NWs grown by CBD. Unlike other dopants such as Al or Ga where the adsorption process is largely driven by predominant electrostatic forces,

Cu incorporates through the *c*-plane top facets of ZnO NWs both in the low-pH (*i.e.* when the  $\text{pH}_0$  is the range of 6.9–7.2) and high-pH (*i.e.* when the  $\text{pH}_0$  is the range of 10.1–10.9) regions. In contrast, Al and Ga do not incorporate in the low-pH region owing to predominant repulsive electrostatic forces associated with the formation of  $\text{Al}^{3+}$  and  $\text{Ga}^{3+}$  ions exhibiting a +3 oxidation state. Al and Ga only incorporate through the *m*-plane sidewalls of ZnO NWs in the high-pH region where attractive electrostatic forces occur,<sup>13,15</sup> in addition to the expected large chemical free energy and very low solvation energy related to the formation of  $\text{Al}(\text{OH}_4)^-$  and  $\text{Ga}(\text{OH}_4)^-$  ion complexes. The particular behavior of Cu can basically be explained by its ability to form the same type of species as Zn when dissolved in an aqueous medium (*i.e.*  $\text{Cu}^{2+}$  and  $\text{Cu}(\text{NH}_3)_4^{2+}$ ), whereas Al and Ga form metal ions with a larger oxidation state in the low-pH region and distinctive hydroxide ion complexes in the high-pH region. However, the formation of the copper oxide phases in the low pH region should be taken into account for nanoscale engineering devices. Moreover, another particularity of Cu in ZnO NWs relies on its ability to form both donor- and acceptor-type defects, whose relative proportion can be tuned with the amount of incorporated Cu. These findings report a more general overview of the incorporation of dopants into ZnO NWs grown by CBD when electrostatic forces are not predominant in the adsorption process of chemical species containing the dopant.

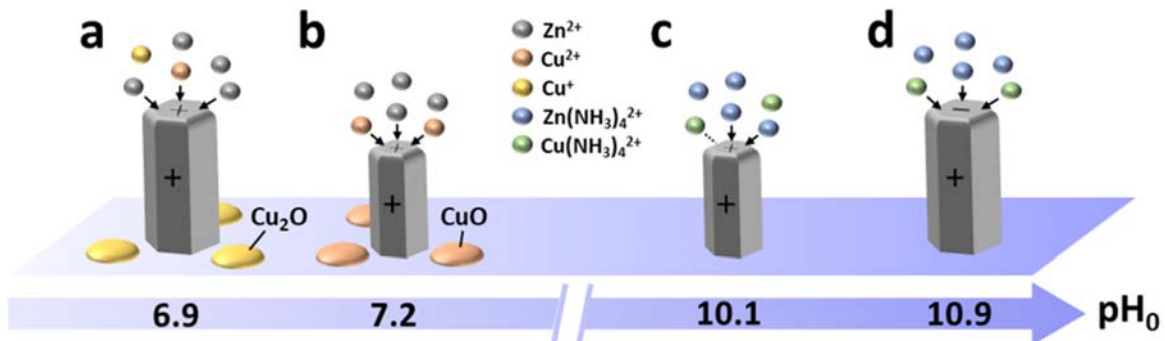


**Figure 9.** Schematic diagram representing the incorporation mechanisms of Cu in ZnO NWs grown by CBD.

#### 4. CONCLUSIONS

In summary, the effects of the addition of  $\text{Cu}(\text{NO}_3)_2$  on the CBD of ZnO NWs grown on Au seed layers using  $\text{pH}_0$  values ranging from 6.9 to 10.9 have thoroughly been investigated. The  $[\text{Cu}(\text{NO}_3)_2]/[\text{Zn}(\text{NO}_3)_2]$  ratio was set to 5 % while the  $\text{pH}_0$  value was tuned through the addition of ammonia. By combining thermodynamic calculations with chemical and structural analyses, we have shown the simultaneous formation of copper oxide nanocrystals along with ZnO NWs on top of the Au seed layer during the CBD process when the  $\text{pH}_0$  value lies in the range of

6.9–7.2 owing to the large supersaturation of Cu species. These nanocrystals take the form of either the Cu<sub>2</sub>O phase at a pH<sub>0</sub> value of 6.9 or the CuO phase when the pH<sub>0</sub> value lies in the range of 7.1–7.2, revealing a change in the oxidation state from +1 to +2 by increasing the pH<sub>0</sub>. No copper oxide phase has been detected in the pH<sub>0</sub> values ranging from 10.1 to 10.9. Moreover, ZnO NWs keep their crystalline quality with no significant incorporation of residual impurities from the chemical precursors. The theoretical Cu(II) and Zn(II) speciation diagrams show that Cu has a very similar chemical behavior to Zn when dissolved in an aqueous medium, as they both form predominantly X<sup>2+</sup> ions (with X = Cu or Zn) when the pH<sub>0</sub> lies in the range of 6.9–7.2, and X(NH<sub>3</sub>)<sub>4</sub><sup>2+</sup> ions when the pH<sub>0</sub> lies in the range of 10.1–10.9. Furthermore, we have identified the Cu incorporation mechanisms into ZnO NWs and their dependence on the pH<sub>0</sub> value. In the low-pH<sub>0</sub> region, Cu<sup>2+</sup> ions compete with Zn<sup>2+</sup> ions for their incorporation through the *c*-plane top facets of ZnO NWs despite repulsive electrostatic interactions owing to their similar ionic structures. However, the amount of incorporated Cu directly depends on the amount of available Cu<sup>2+</sup> ions, which is very low at a pH<sub>0</sub> value of 6.9 and becomes significant when the pH<sub>0</sub> lies in the range of 7.1–7.2. In the high-pH<sub>0</sub> region, Cu(NH<sub>3</sub>)<sub>4</sub><sup>2+</sup> ions also compete with Zn(NH<sub>3</sub>)<sub>4</sub><sup>2+</sup> ions for their incorporation through the *c*-plane top facets of ZnO NWs despite repulsive electrostatic interactions owing to their similar ionic structures. Interestingly, at a pH<sub>0</sub> value of 10.9, the *c*-plane top facets of ZnO NWs become negatively charged creating additional attractive electrostatic interactions with Cu(NH<sub>3</sub>)<sub>4</sub><sup>2+</sup> ions, which favors the more significant incorporation of Cu. The present findings reveal the distinctive incorporation mechanisms of Cu as compared to other dopants such as Al or Ga and generalize the strategy to dope ZnO NWs by CBD beyond the only consideration of electrostatic forces involved in the adsorption process of dopant species. They should be taken into account to achieve Cu-doped ZnO NWs with tunable optical and electrical properties.

## SUPPORTING INFORMATION

Thermodynamic constants used in Visual MINTEQ, in situ pH measurements during CBD, and temperature-dependent Raman spectra of ZnO NWs grown at a pH<sub>0</sub> of 7.1 and with a Cu(NO<sub>3</sub>)<sub>2</sub>/Zn(NO<sub>3</sub>)<sub>2</sub> ratio of 5 % (PDF)

## AUTHOR INFORMATION

### Corresponding authors

\*E-mail: [bassem.salem@cea.fr](mailto:bassem.salem@cea.fr)

\*E-mail: [vincent.consonni@grenoble-inp.fr](mailto:vincent.consonni@grenoble-inp.fr)

## **ORCID**

Clément Lausecker: 0000-0001-8139-4029

Bassem Salem: 0000-0001-8038-3205

Xavier Baillin: 0000-0001-6750-5300

Odette Chaix-Pluchery: 0000-0001-9699-7084

Vincent Consonni: 0000-0003-0171-8746

## **Notes**

The authors declare no competing financial interests

## **ACKNOWLEDGEMENTS**

This work was partially supported by the LabEx Minos under the contract ANR-10-LABX-55-01 and by the EquipEx IMPACT program, managed by the French Research National Agency (ANR-10-EQPX-33). C.L. received a doctoral fellowship from the LabEx Minos. V.C. also acknowledges the financial support from the French Research National Agency through the projects ROLLER (ANR-17-CE09-0033) and DOSETTE (ANR-17-CE24-0003). This work has further benefited from some of the characterization equipment of the Grenoble INP–CMTC platform and has partially been supported by the French Research National Agency in the framework of the “Investissement d’avenir” program (ANR-15-IDEX-02) through the project CDP NEED.

## REFERENCES

- (1) Wang, Z. L. Towards Self-Powered Nanosystems: From Nanogenerators to Nanopiezotronics. *Adv. Funct. Mater.* **2008**, *18*, 3553–3567.
- (2) Willander, M.; Nur, O.; Zhao, Q. X.; Yang, L. L.; Lorenz, M.; Cao, B. Q.; Zúñiga Pérez, J.; Czekalla, C.; Zimmermann, G.; Grundmann, M.; Bakin, A.; Behrends, A.; Al-Suleiman, M.; El-Shaer, A.; Che Mofor, A.; Postels, B.; Waag, A.; Boukos, N.; Travlos, A.; Kwack, H. S.; Guinard, J.; Le Si Dang, D. Zinc Oxide Nanorod Based Photonic Devices: Recent Progress in Growth, Light Emitting Diodes and Lasers. *Nanotechnology* **2009**, *20*, 332001.
- (3) Tian, W.; Lu, H.; Li, L. Nanoscale Ultraviolet Photodetectors Based on Onedimensional Metal Oxide Nanostructures. *Nano Res.* **2015**, *8*, 382–405.
- (4) Consonni, V.; Briscoe, J.; Kärber, E.; Li, X.; Cossuet, T. ZnO Nanowires for Solar Cells: A Comprehensive Review. *Nanotechnology* **2019**, *30*, 362001.
- (5) Zhu, L.; Zeng, W. Room-Temperature Gas Sensing of ZnO-Based Gas Sensor: A Review. *Sens. Actuators Phys.* **2017**, *267*, 242–261.
- (6) Xu, S.; Wang, Z. L. One-Dimensional ZnO Nanostructures: Solution Growth and Functional Properties. *Nano Res.* **2011**, *4*, 1013–1098.
- (7) Vayssieres, L.; Keis, K.; Lindquist, S.-E.; Hagfeldt, A. Purpose-Built Anisotropic Metal Oxide Material: 3D Highly Oriented Microrod Array of ZnO. *J. Phys. Chem. B* **2001**, *105*, 3350–3352.
- (8) Parize, R.; Garnier, J. D.; Appert, E.; Chaix-Pluchery, O.; Consonni, V. Effects of Polyethylenimine and Its Molecular Weight on the Chemical Bath Deposition of ZnO Nanowires. *ACS Omega* **2018**, *3*, 12457–12464.
- (9) Liu, B.; Zeng, H. C. Hydrothermal Synthesis of ZnO Nanorods in the Diameter Regime of 50 nm. *J. Am. Chem. Soc.* **2003**, *125*, 4430–4431.
- (10) Xu, L.; Guo, Y.; Liao, Q.; Zhang, J.; Xu, D. Morphological Control of ZnO Nanostructures by Electrodeposition. *J. Phys. Chem. B* **2005**, *109*, 13519–13522.
- (11) Kim, J. H.; Andeen, D.; Lange, F. F. Hydrothermal Growth of Periodic, Single-Crystal ZnO Microrods and Microtunnels. *Adv. Mater.* **2006**, *18*, 2453–2457.

- (12) Joo, J.; Chow, B. Y.; Prakash, M.; Boyden, E. S.; Jacobson, J. M. Face-Selective Electrostatic Control of Hydrothermal Zinc Oxide Nanowire Synthesis. *Nat. Mater.* **2011**, *10*, 596–601.
- (13) Verrier, C.; Appert, E.; Chaix-Pluchery, O.; Rapenne, L.; Rafhay, Q.; Kaminski-Cachopo, A.; Consonni, V. Effects of the pH on the Formation and Doping Mechanisms of ZnO Nanowires Using Aluminum Nitrate and Ammonia. *Inorg. Chem.* **2017**, *56*, 13111–13122.
- (14) Verrier, C.; Appert, E.; Chaix-Pluchery, O.; Rapenne, L.; Rafhay, Q.; Kaminski-Cachopo, A.; Consonni, V. Tunable Morphology and Doping of ZnO Nanowires by Chemical Bath Deposition Using Aluminum Nitrate. *J. Phys. Chem. C* **2017**, *121*, 3573–3583.
- (15) Gaffuri, P.; Appert, E.; Chaix-Pluchery, O.; Rapenne, L.; Salaün, M.; Consonni, V. The Path of Gallium from Chemical Bath into ZnO Nanowires: Mechanisms of Formation and Incorporation. *Inorg. Chem.* **2019**, *58*, 10269–10279.
- (16) Degen, A.; Kosec, M. Effect of pH and Impurities on the Surface Charge of Zinc Oxide in Aqueous Solution. *J. Eur. Ceram. Soc.* **2000**, *20*, 667–673.
- (17) Tian, G.; Xiong, D.; Su, Y.; Yang, T.; Gao, Y.; Yan, C.; Deng, W.; Jin, L.; Zhang, H.; Fan, X.; Wang, C.; Deng, W.; Yang, W. Understanding the Potential Screening Effect through the Discretely Structured ZnO Nanorods Piezo Array. *Nano Lett.* **2020**, *20*, 4270–4277.
- (18) McCluskey, M. D.; Jokela, S. J. Defects in ZnO. *J. Appl. Phys.* **2009**, *106*, 071101.
- (19) Yan, Y.; Al-Jassim, M. M.; Wei, S.-H. Doping of ZnO by Group-IB Elements. *Appl. Phys. Lett.* **2006**, *89*, 181912.
- (20) Huang, D.; Zhao, Y.-J.; Chen, D.-H.; Shao, Y.-Z. Magnetism and Clustering in Cu Doped ZnO. *Appl. Phys. Lett.* **2008**, *92*, 182509.
- (21) Qiu, H.; Gallino, F.; Di Valentin, C.; Wang, Y. Shallow Donor States Induced by In-Diffused Cu in ZnO: A Combined HREELS and Hybrid DFT Study. *Phys. Rev. Lett.* **2011**, *106*, 066401.
- (22) Wang, R.-C.; Lin, H.-Y. Cu Doped ZnO Nanoparticle Sheets. *Mater. Chem. Phys.* **2011**, *125*, 263–266.
- (23) Polat, İ.; Yılmaz, S.; Altın, İ.; Bacaksız, E.; Sökmen, M. The Influence of Cu-Doping on Structural, Optical and Photocatalytic Properties of ZnO Nanorods. *Mater. Chem. Phys.* **2014**, *148*, 528–532.

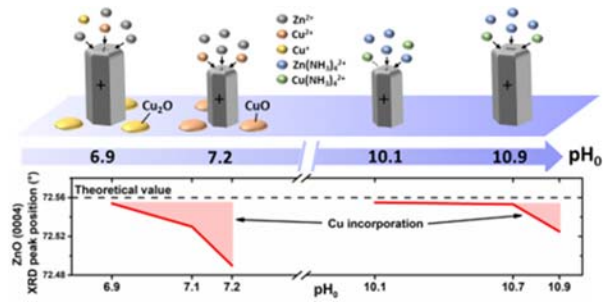
- (24) Raja, M.; Muthukumarasamy, N.; Velauthapillai, D.; Balasundaraprabhu, R. Influence of Copper on the Morphology and Properties of One Dimensional ZnO Nanorod Structures. *Superlattices Microstruct.* **2014**, *72*, 102–110.
- (25) Hassanpour, A.; Guo, P.; Shen, S.; Bianucci, P. The Effect of Cation Doping on the Morphology, Optical and Structural Properties of Highly Oriented Wurtzite ZnO-Nanorod Arrays Grown by a Hydrothermal Method. *Nanotechnology* **2017**, *28*, 435707.
- (26) Mwankemwa, B. S.; Legodi, M. J.; Mlambo, M.; Nel, J. M.; Diale, M. Structural, Morphological, Optical and Electrical Properties of Schottky Diodes Based on CBD Deposited ZnO:Cu Nanorods. *Superlattices Microstruct.* **2017**, *107*, 163–171.
- (27) Rakhsha, A. H.; Abdizadeh, H.; Pourshaban, E.; Golobostanfard, M. R.; Mastelaro, V. R.; Montazerian, M. Ag and Cu Doped ZnO Nanowires: A pH-Controlled Synthesis via Chemical Bath Deposition. *Materialia* **2019**, *5*, 100212.
- (28) Chow, L.; Lupan, O.; Chai, G.; Khallaf, H.; Ono, L. K.; Roldan Cuenya, B.; Tiginyanu, I. M.; Ursaki, V. V.; Sontea, V.; Schulte, A. Synthesis and Characterization of Cu-Doped ZnO One-Dimensional Structures for Miniaturized Sensor Applications with Faster Response. *Sens. Actuators Phys.* **2013**, *189*, 399–408.
- (29) Iribarren, A.; Hernández-Rodríguez, E.; Maqueira, L. Structural, Chemical and Optical Evaluation of Cu-Doped ZnO Nanoparticles Synthesized by an Aqueous Solution Method. *Mater. Res. Bull.* **2014**, *60*, 376–381.
- (30) Shabannia, R. Synthesis and Characterization of Cu-Doped ZnO Nanorods Chemically Grown on Flexible Substrate. *J. Mol. Struct.* **2016**, *1118*, 157–160.
- (31) Shannon, R. D. Revised Effective Ionic Radii and Systematic Studies of Interatomic Distances in Halides and Chalcogenides. *Acta Crystallogr. Sect. A* **1976**, *A32*, 751–767.
- (32) Hou, D. L.; Ye, X. J.; Meng, H. J.; Zhou, H. J. Magnetic Properties of N-Type Cu-Doped ZnO Thin Films. *Appl Phys Lett* **2007**, *90*, 142502.
- (33) Shuai, M.; Liao, L.; Lu, H. B.; Zhang, L.; Li, J. C.; Fu, D. J. Room-Temperature Ferromagnetism in Cu<sup>+</sup> Implanted ZnO Nanowires. *J. Phys. Appl. Phys.* **2008**, *41*, 135010.
- (34) Liu, H.; Yang, J.; Hua, Z.; Zhang, Y.; Yang, L.; Xiao, L.; Xie, Z. The Structure and Magnetic Properties of Cu-Doped ZnO Prepared by Sol–Gel Method. *Appl. Surf. Sci.* **2010**, *256*, 4162–4165.

- (35) Chakraborti, D.; Narayan, J.; Prater, J. T. Room Temperature Ferromagnetism in  $Zn_{1-x}Cu_xO$  Thin Films. *Appl. Phys. Lett.* **2007**, *90*, 062504.
- (36) Wang, X.; Xu, J. B.; Cheung, W. Y.; An, J.; Ke, N. Aggregation-Based Growth and Magnetic Properties of Inhomogeneous Cu-Doped ZnO Nanocrystals. *Appl. Phys. Lett.* **2007**, *90*, 212502.
- (37) Xing, G. Z.; Yi, J. B.; Tao, J. G.; Liu, T.; Wong, L. M.; Zhang, Z.; Li, G. P.; Wang, S. J.; Ding, J.; Sum, T. C.; Huan, C. H. A.; Wu, T. Comparative Study of Room-Temperature Ferromagnetism in Cu-Doped ZnO Nanowires Enhanced by Structural Inhomogeneity. *Adv. Mater.* **2008**, *20*, 3521–3527.
- (38) Fu, M.; Li, Y.; Wu, S.; Lu, P.; Liu, J.; Dong, F. Sol–Gel Preparation and Enhanced Photocatalytic Performance of Cu-Doped ZnO Nanoparticles. *Appl. Surf. Sci.* **2011**, *258*, 1587–1591.
- (39) Wang, Z. L.; Wu, W.; Falconi, C. Piezotronics and Piezo-Phototronics with Third-Generation Semiconductors. *MRS Bull.* **2018**, *43*, 922–927.
- (40) Wen, X.; Wu, W.; Ding, Y.; Wang, Z. L. Seedless Synthesis of Patterned ZnO Nanowire Arrays on Metal Thin Films (Au, Ag, Cu, Sn) and Their Application for Flexible Electromechanical Sensing. *J. Mater. Chem.* **2012**, *22*, 9469.
- (41) Lausecker, C.; Salem, B.; Baillin, X.; Roussel, H.; Sarigiannidou, E.; Bassani, F.; Appert, E.; Labau, S.; Consonni, V. Formation Mechanisms of ZnO Nanowires on Polycrystalline Au Seed Layers for Piezoelectric Applications. *Nanotechnology* **2019**, *30*, 345601.
- (42) Willander, M.; Yang, L. L.; Wadeasa, A.; Ali, S. U.; Asif, M. H.; Zhao, Q. X.; Nur, O. Zinc Oxide Nanowires: Controlled Low Temperature Growth and Some Electrochemical and Optical Nano-Devices. *J Mater Chem* **2009**, *19*, 1006–1018.
- (43) Lausecker, C.; Salem, B.; Baillin, X.; Consonni, V. Modeling the Elongation of Nanowires Grown by Chemical Bath Deposition Using a Predictive Approach. *J. Phys. Chem. C* **2019**, *123*, 29476–29483.
- (44) Terasako, T.; Ohnishi, K.; Okada, H.; Obara, S.; Yagi, M. Possibility of Selective and Morphology-Controlled Growth of CuO and Cu<sub>2</sub>O Films. *Thin Solid Films* **2017**, *644*, 146–155.
- (45) Liang, H.; Upmanyu, M.; Huang, H. Size-Dependent Elasticity of Nanowires: Nonlinear Effects. *Phys. Rev. B* **2005**, *71*, 241403.
- (46) Hu, J.; Liu, X. W.; Pan, B. C. A Study of the Size-Dependent Elastic Properties of ZnO Nanowires and Nanotubes. *Nanotechnology* **2008**, *19*, 285710.

- (47) Bundesmann, C.; Ashkenov, N.; Schubert, M.; Spemann, D.; Butz, T.; Kaidashev, E. M.; Lorenz, M.; Grundmann, M. Raman Scattering in ZnO Thin Films Doped with Fe, Sb, Al, Ga, and Li. *Appl. Phys. Lett.* **2003**, *83*, 1974–1976.
- (48) Manjón, F. J.; Marí, B.; Serrano, J.; Romero, A. H. Silent Raman Modes in Zinc Oxide and Related Nitrides. *J. Appl. Phys.* **2005**, *97*, 053516.
- (49) Lupan, O.; Pauporté, T.; Viana, B.; Aschehoug, P. Electrodeposition of Cu-Doped ZnO Nanowire Arrays and Heterojunction Formation with p-GaN for Color Tunable Light Emitting Diode Applications. *Electrochimica Acta* **2011**, *56*, 10543–10549.
- (50) Zhao, M.; Wang, X.; Ning, L.; Jia, J.; Li, X.; Cao, L. Electrospun Cu-Doped ZnO Nanofibers for H<sub>2</sub>S Sensing. *Sens. Actuators B Chem.* **2011**, *156*, 588–592.
- (51) Cuscó, R.; Alarcón-Lladó, E.; Ibáñez, J.; Artús, L.; Jiménez, J.; Wang, B.; Callahan, M. J. Temperature Dependence of Raman Scattering in ZnO. *Phys. Rev. B* **2007**, *75*, 165202.
- (52) Sander, T.; Reindl, C. T.; Giar, M.; Eifert, B.; Heinemann, M.; Heiliger, C.; Klar, P. J. Correlation of Intrinsic Point Defects and the Raman Modes of Cuprous Oxide. *Phys. Rev. B* **2014**, *90*, 045203.
- (53) Kliche, G.; Popovic, Z. V. Far-Infrared Spectroscopic Investigations on CuO. *Phys. Rev. B* **1990**, *42*, 10060–10066.
- (54) XPS Interpretation of Copper <https://xpssimplified.com/elements/copper.php> (accessed Dec 15, 2020).
- (55) James, R. O.; Healy, T. W. Adsorption of Hydrolyzable Metal Ions at the Oxide—Water Interface. III. A Thermodynamic Model of Adsorption. *J. Colloid Interface Sci.* **1972**, *40*, 65–81.
- (56) Fuerstenau, D. W.; Osseo-Asare, K. Adsorption of Copper, Nickel, and Cobalt by Oxide Adsorbents from Aqueous Ammoniacal Solutions. *J. Colloid Interface Sci.* **1987**, *118*, 524–542.
- (57) Valtiner, M.; Borodin, S.; Grundmeier, G. Stabilization and Acidic Dissolution Mechanism of Single-Crystalline ZnO(0001) Surfaces in Electrolytes Studied by In-Situ AFM Imaging and Ex-Situ LEED. *Langmuir* **2008**, *24*, 5350–5358.
- (58) Kunze, C.; Valtiner, M.; Michels, R.; Huber, K.; Grundmeier, G. Self-Localization of Polyacrylic Acid Molecules on Polar ZnO(0001)–Zn Surfaces. *Phys. Chem. Chem. Phys.* **2011**, *13*, 12959.

- (59) Cossuet, T.; Donatini, F.; Lord, A. M.; Appert, E.; Pernot, J.; Consonni, V. Polarity-Dependent High Electrical Conductivity of ZnO Nanorods and Its Relation to Hydrogen. *J. Phys. Chem. C* **2018**, *122*, 22767–22775.
- (60) Villafuerte, J.; Donatini, F.; Kioseoglou, J.; Sarigiannidou, E.; Chaix-Pluchery, O.; Pernot, J.; Consonni, V. Zinc Vacancy–Hydrogen Complexes as Major Defects in ZnO Nanowires Grown by Chemical Bath Deposition. *J. Phys. Chem. C* **2020**, *124*, 16652–16662.

## TOC Graphic



## TOC Synopsis

To control the electrical properties of ZnO nanowires grown by chemical bath deposition, the effects of the addition of copper nitrate in the chemical bath are investigated in detail. By combining thermodynamic simulations with chemical and structural characterizations, we provide a detailed analysis of the incorporation mechanisms of Cu into ZnO nanowires, which are considered beyond the only electrostatic forces usually driving the incorporation of dopants such as Al or Ga.